Galaxy Publication

Synthesis, Structural Characterization, DFT Studies, and Anticancer Activity of Benzimidazole-derived Imines with Cu (II) and Co (III) Complexes

Chloe Martin[1]*, Benjamin Wright[1], Oliver Scott[1]

[1]Department of Pharmaceutical Sciences, School of Pharmacy, University of Manchester, Manchester, United Kingdom.

*E-mail ✉ chloe.martin@outlook.com

ABSTRACT

Recent advancements in coordination chemistry and its biological applications have made a significant impact in chemical biology. Motivated by this progress, we have synthesized a new benzimidazole-based imine ligand, 2-((E)-((1H-benzo[d]-2-yl)methylimino)methyl)-4-fluorophenol (HBMF), and investigated its complexes with Co(III) and Cu(II) ions. The metal complexes (C1–C4) were prepared in two distinct stoichiometries: a 2:1 (HBMF: metal ion) ratio and a 1:1:1 ratio (HBMF: metal ion: 1,10-phenanthroline). Comprehensive structural characterization of these compounds was performed using FT-IR, UV-Vis, NMR, mass spectrometry, and elemental analysis. To further understand their properties, we employed both first-principles computational methods and molecular dynamics simulations. Quantum mechanical calculations using density functional theory (DFT) were applied to explore the reactive and spectroscopic features of the HBMF ligand and its metal complexes, while molecular dynamics simulations with the OPLS4 force field were used to investigate the ligand's reactivity in aqueous environments. The biological activity of the compounds was assessed in vitro against several cancer cell lines, including A549, Ehrlich-Lettre ascites carcinoma (EAC), SIHA, and NIH3T3. Among the metal complexes, compound C4 (C27H23Cl2CoFN5O3) demonstrated the strongest anti-proliferative effect against EAC cells, with an impressive IC50 of 10 µM, outperforming both the parent ligand and other metal complexes. Hematological assessments, including the measurement of alkaline phosphatase, creatinine, urea, RBC, and WBC levels, revealed notable results. Additionally, C4's effect on angiogenesis was evaluated by stimulating neovascularization through rVEGF165, with comparisons to non-tumor models. In vivo studies were conducted on EAC cells, where animals were treated with doses of 50 and 75 mg/kg, and the tumor parameters were carefully analyzed.

Keywords: DFT, Benzimidazole, Antitumor activity, Schiff base

Introduction

Schiff bases are well-established functional groups in medicinal chemistry, known for their broad range of pharmacological activities [1]. Due to their synthetic versatility, structural stability, and effective coordination with metal ions, Schiff bases are regarded as highly versatile ligands in coordination chemistry [2]. However, many chemotherapeutic agents used in clinical settings exhibit high toxicity and lack specificity for cancer cells [3]. The discovery of antitumor activity in several imine-based coordination complexes highlights the importance of targeting specific cancer cells. Modifying and optimizing N-heterocyclic Schiff base complexes with transition metals is a key strategy for studying their potential therapeutic applications [4].

In recent years, there has been a growing interest in copper and cobalt complexes, largely due to the belief that these metals are endogenous and possess lower toxicity. It is widely recognized that the antitumor effects of copper and cobalt-based compounds are influenced by the nature of the ligands and donor atoms coordinating to the metal centers. Benzimidazole-based N-heterocyclic imine ligands, for example, serve as effective chelating agents for

transition metals [5]. Transition metal complexes containing benzimidazole-imine ligands have demonstrated diverse pharmacological properties, including antibacterial, antifungal, anti-inflammatory, antioxidant, and anticancer activities [6]. Additionally, platinum-based metal complexes have led the way in chemotherapy, providing insights into the development of future transition metal-based therapeutic agents [7].

The role of cobalt in coordination chemistry is particularly intriguing, as its biochemistry is critical for processes such as red blood cell formation, DNA synthesis, and the proper functioning of the brain and nervous system through cobalamin and its derivatives [8]. Cobalt's involvement in amino acid and fatty acid metabolism has also been widely documented [9], sparking interest in cobalt-containing imine-based complexes as potential alternatives to cisplatin with reduced toxicity [10].

In modern research, computational tools have become indispensable for identifying optimal candidates for pharmaceutical and material science applications, as well as for understanding the mechanisms behind their activities [11, 12]. Among these tools, quantum-mechanical methods, particularly density functional theory (DFT), are highly effective in analyzing the reactivity of molecular systems while maintaining an optimal balance between accuracy and computational cost [13]. Additionally, molecular dynamics (MD) simulations are invaluable for studying molecular interactions with solvents and for handling complex molecular systems [14]. Combining DFT and MD methods provides a clearer picture of the reactivity of newly synthesized molecules. In this study, we employed these computational techniques to better understand the reactivity of the newly synthesized HBMF ligand and its cobalt and copper complexes.

The main objective of this paper is to present the synthesis, characterization, and pharmacological evaluation of the HBMF ligand (2-((E)-((1H-benzo[d]-2-yl)methylimino)methyl)-4-fluorophenol) and its Co(III) and Cu(II) complexes. In-depth computational studies, along with in vitro and in vivo assays based on IC50 values, were conducted to evaluate the anticancer activity of these complexes. Additionally, the DNA binding affinity and DNA cleavage properties of the complexes were investigated.
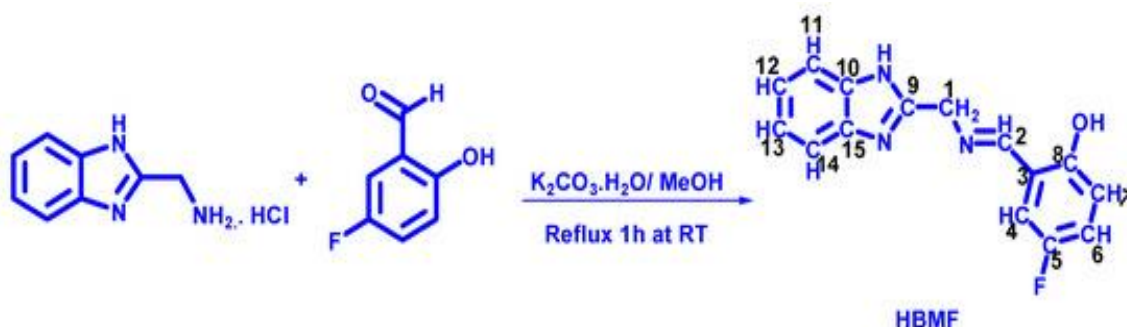
Materials and Methods

All chemicals and solvents used in this study were sourced commercially and used as received, without any further purification. The 2-(aminomethyl)benzimidazole dihydrochloride, 5-fluorosalicylaldehyde, and 1,10-phenanthroline monohydrate were purchased from Sigma Aldrich, Dresden, Germany. The melting points of the ligand and complexes were determined using an ELICO-3210 apparatus; these values were uncorrected. Elemental analysis (CHNS) of the compounds was conducted on a Perkin-Elmer 240 elemental analyzer. FT-IR spectra were collected between 4000 and 400 cm−1 with a Bruker IFS66V spectrometer, using KBr pellets for the ligand and the Nujol-mull method for the complexes. Proton and carbon NMR spectra were recorded using a Bruker NMR spectrometer, with CDCl3 as the solvent and tetramethylsilane (TMS) as the internal standard. The IR spectra of the synthesized heterocyclic base and its metal complexes were measured on a Perkin-Elmer spectrometer. Electronic spectra were obtained using an ELICO SL117 double beam spectrophotometer and a quartz cell for both the ligand and its complexes. For the copper complexes, their paramagnetic behavior was studied by electron spin resonance (ESR) at 77 K using a JEOL X-Band spectrometer under liquid nitrogen, with tetracyanoethylene (TCNE) as the g-marker. Mass spectrometry data were recorded on a Shimadzu 2010 EV LC-MS spectrometer. The molar conductance of the Schiff base metal complexes was measured with an Elico CM-180 conductometer, using a cell constant of 1. Thermal analysis of the complexes was performed using a TGA-Q50 instrument, heating at a rate of 10 °C/min to a maximum temperature of 800 °C.

Synthesis of 2-((E)-((1H-benzo[d]-2-yl)methylimino)methyl)-4-fluorophenol (HBMF)

The synthesis of HBMF is illustrated in Scheme 1. First, 2-(aminomethyl)benzimidazole hydrochloride (0.100 g, 0.4543 mmol) was neutralized with an aqueous potassium carbonate solution (0.0753 g, 0.5451 mmol). This mixture was then combined with a methanolic solution of 5-fluorosalicylaldehyde (0.0630 g, 0.4543 mmol). The reaction was carried out at room temperature under magnetic stirring, leading to the formation of a yellow precipitate. The precipitate was filtered, washed with water and petroleum ether, and then dried under vacuum. The reaction's progress was monitored by thin layer chromatography (TLC) using a chloroform-methanol solvent mixture (9:1 ratio) on pre-coated silica gel plates. The resulting Schiff base was found to be insoluble in water but soluble in solvents like methanol and DMSO.

Elemental analysis of the product (HBMF, C15H11FN3O) was consistent with the following values: Calculated (%): C, 62.91; H, 4.33; F, 7.05; N, 14.59; O, 5.90. Found (%): C, 62.95; H, 4.36; F, 7.09; N, 14.65; O, 5.94. The proton NMR spectrum (CDCl3, 400 MHz) showed peaks at 5.09 (s, 2H, CH2), 6.86 (dd, 2H, Ar-H), 7.04–7.06 (t, 1H, Ar-H), 7.25 (d, 2H, Ar-H), 7.57 (d, 1H, Ar-H), 7.58 (d, 1H, Ar-H), 8.41 (s, 1H, N=CH), and 12.80 (broad, 1H, Imidazole NH). The –OH group of the phenolic structure did not show up due to the electron-withdrawing effect of the fluorine atom on the aromatic ring. The 13C NMR (CDCl3, 100 MHz) spectrum displayed signals at 57.334 (C1), 115.95 (C11), 116.79 (C14), 117.02 (C7), 118.08 (C4), 118.15 (C12), 118.92 (C13), 120.17 (C6), 120.41 (C3), 122.96 (C10), 123.15 (C15), 150.27 (C9), 154.31 (C8), 156.78 (C5), and 167.67 (C2) ppm. The ESI-LCMS analysis showed a mass peak at m/z: calculated for C15H11FN3O, 270.27; found at 271.110 (M + 1).

Scheme 1. Synthesis route of the Schiff base ligand (HBMF).

Synthesis of Co (III) and Cu(II) complexes (1:2 Molar Ratio) – complexes C1 and C3

To synthesize the complexes C1 and C3, a hot methanolic solution of the metal salts (CoCl2·6H2O and CuCl2·2H2O) was mixed with a methanolic solution of the ligand (HBMF). This reaction mixture was refluxed at 65°C for six hours, yielding brown and green solid complexes corresponding to Co(III) and Cu(II), respectively.

C1: [Cu(BMF)2] Yield = 78%; melting point: 255–258°C; green color Elemental analysis for C30H22CuF2N6O2: Calculated (%): C: 60.05, H: 3.66, N: 14.00, Cu: 10.59, F: 6.33, O: 5.33 Found (%): C: 60.06, H: 3.69, N: 13.99, Cu: 10.58, F: 6.32, O: 5.32

C3: [Co(BMF)2]Cl Yield = 71%; melting point: 281–286°C; brown color Elemental analysis for C30H22ClCoF2N6O2: Calculated (%): C: 57.14, H: 3.49, Cl: 5.55, Co: 9.36, F: 6.03, N: 13.33, O: 5.07 Found (%): C: 57.13, H: 3.51, Cl: 5.61, Co: 9.33, F: 6.01, N: 13.31, O: 5.06

Synthesis of Co(III) and Cu(II) complexes (1:1:1 molar ratio) – complexes C2 and C4

For the synthesis of complexes C2 and C4, a methanolic solution containing the metal chlorides (CoCl2·6H2O and CuCl2·2H2O) was added to a methanolic solution of the ligand (HBMF) and 1,10-phenanthroline. The reaction mixture was heated and refluxed at 65°C for 6 hours, producing brown and green solid complexes corresponding to Co(III) and Cu(II).

C2: [Cu(BMF)(phen)Cl]·3H2O Yield = 69%; melting point: 303–308°C; green color Elemental analysis for C30H25ClCuFN5O4: Calculated (%): C: 55.01, H: 4.37, Cl: 6.02, Cu: 10.69, F: 3.16, N: 11.83, O: 10.72 Found (%): C: 54.04, H: 4.17, Cl: 5.88, Cu: 10.53, F: 3.14, N: 11.60, O: 10.60

C4: [Co(BMF)(phen)Cl]Cl·2H2O Yield = 72%; melting point: 311–316°C; brown color Elemental analysis for C27H23Cl2CoFN5O3: Calculated (%): C: 52.97, H: 3.86, Cl: 11.59, Co: 9.77, F: 3.14, N: 11.51, O: 7.89 Found (%): C: 52.91, H: 3.76, Cl: 11.51, Co: 9.56, F: 3.08, N: 11.36, O: 7.78

Pharmacological studies

The pharmacological properties of the complexes were evaluated through in vitro and in vivo assays to assess their potential cellular interactions. Initially, the compounds were tested for cytotoxicity and inhibition of cell proliferation using A459, EAC, SIHA, and NIH3T3 cell lines (ATCC® HTB-22™, Manassas, VA, USA). Complex C4 was found to exhibit substantial anti-proliferative activity against EAC cell lines, prompting further studies on its anti-cancer potential, as reported in previous literature [15].

In vitro studies on cell culture

Cell cultures of A549, EAC, SIHA, and NIH3T3 were maintained under controlled laboratory conditions. The cells were grown in Dulbecco's Modified Eagle Medium (DMEM) (Gibco-Invitrogen, Austin, TX, USA), supplemented with fetal bovine serum (FBS) (Invitrogen, Waltham, MA, USA), penicillin-streptomycin, and sodium bicarbonate (0.40%). The cultures were incubated at 37°C with 97% humidity and 90% air atmosphere. For testing anti-proliferative and cytotoxic effects, the complexes (C1–C4) and the parent ligand HBMF (10 μM concentration) dissolved in DMSO were applied. The MTT assay, as described previously [16], was used to measure the anti-proliferative activity, and 5-fluorouracil was used as a positive control.

MTT assay for cell proliferation
The anti-proliferative activity of HBMF, its complexes, and 5-fluorouracil was assessed using the MTT assay. Cells were incubated with the compounds for 48 hours, and cell proliferation was evaluated by adding 5 mg/mL of MTT reagent [17], followed by analysis of the resulting color change, which reflects cell viability.

Ethical approval for animal studies
Swiss albino male mice (weight range: 25–27 g) were housed under standard laboratory conditions with free access to food and water. All animal experimentation was approved by the Institutional Animal Ethics Committee, National College of Pharmacy, Shimoga, India, and adhered to the guidelines of the Committee for the Purpose of Control and Supervision of Experiments on Animals (CPCSEA) (NCP/IAEC/101/05/2012-13).

Hematological investigations
Standard techniques, including cell dilution and hemocytometry, were used to assess hematological parameters (e.g., WBC, RBC, alkaline phosphatase, urea, and creatinine) in both normal and EAC-bearing mice. Mice were divided into 10 groups (n = 4 per group). Tumors were transplanted and treatments initiated 24 hours later. Group 1 mice remained untreated; Group 2 received a standard dose of Bleomycin (0.3 mg/kg i.p.); Groups 3–5 were treated with complex C4 at escalating doses of 2.5 mg/kg, 5.0 mg/kg, and 10 mg/kg, respectively, for 10 consecutive days. Blood samples were collected every 5 days for analysis [18]. In non-tumor-bearing mice, Groups 1–4 received complex C4 at similar doses to evaluate its effect on hematological parameters.

In vivo antitumor activity
The antitumor effect of complex C4 was studied in EAC-bearing mice (Accession number: PF0041). EAC cells (1×10^6 cells per mouse) were introduced into the peritoneal cavity to induce tumors. A total of 40 mice were used and divided into four groups. Complex C4, dissolved in 1% DMSO, was administered intraperitoneally (i.p.) at 50 mg/kg (Group C) and 75 mg/kg (Group D) on alternate days. Group B received DMSO as a vehicle control. The animals were monitored for survival throughout the study.

Chorioallantoic membrane (CAM) assay
To assess the anti-angiogenic effects of complex C4, the CAM assay was conducted on fertilized eggs over 15 days, following the method described previously [19]. The impact of C4 at doses of 50 mg/kg and 75 mg/kg on angiogenesis induced by rVEGF165 was analyzed. Microvessel density (MVD) was measured, and images were captured using a Sony DSC-W610 camera.

Microvessel density (MVD) measurement
MVD was determined by assessing the extent of angiogenesis in the peritoneum of tumor-bearing mice, using H&E staining techniques as previously described [19]. The effects of complex C4 on angiogenesis in the peritoneum were documented through light microscopy and MVD analysis in formalin-fixed tissue [20].

Computational methodology
The computational analysis of the HBMF ligand and its complexes with Cu and Co ions was conducted using a combination of Density Functional Theory (DFT), Time-Dependent DFT (TD-DFT), and Molecular Dynamics (MD) simulations. Initially, the molecular structure of HBMF was analyzed for different conformations using the OPLS4 force field, implemented in the MacroModel software [21]. Conformers were then optimized using the B3LYP functional [22] and 6-31 G(d,p) basis set [23]. From these, the ten lowest energy conformations were

selected and re-optimized with higher accuracy in self-consistent field calculations. Once the optimal conformation was identified, further computations were performed.

For the metal complexes of HBMF, 2D structures were designed using the Maestro program. These structures were then converted into 3D models, followed by force field minimization to ensure reasonable bond lengths. The initial geometries were optimized at the quantum level using the extended tight binding (xTB) model [24], with input files generated using the atomistica. online xTB tool. These initial structures were optimized further with the B3LYP functional and MIDIXL basis set [25]. After optimization, frequency calculations confirmed that the geometries corresponded to the true minima, with all calculated frequencies being positive.

Organometallic computations for the complexes were carried out using ligand field theory, incorporating d-d repulsion to determine the metal d orbital distribution. A unique occupation state for the metal's d orbitals was identified below a threshold of 0.01 Hartree, assuming a doublet multiplicity. For each complex, metal ions and the first and second ligands were assigned formal charges of +2, −1, and −1, respectively.

To explore the electronic properties, the optimized structures of HBMF and its complexes were further investigated using the M06-2X functional [26] and the LACVP(d,p) basis set [27]. These calculations aimed to provide insights into the frontier molecular orbitals and quantum molecular descriptors like molecular electrostatic potential (MEP) and average local ionization energy (ALIE). TD-DFT calculations were performed using the CAM-B3LYP functional [28] to examine excited state properties.

MD simulations, conducted with the OPLS4 force field [29], utilized a simulation time of 10 ns in an NPT ensemble. One ligand molecule was placed in a cubic simulation box containing approximately 2000 water molecules modeled using the SPC water model [30]. The resulting simulation trajectories were analyzed to calculate radial distribution functions (RDF).

All the DFT and TD-DFT calculations were performed using the Jaguar software [31, 32], while MD simulations were executed using the Desmond software [33]. The Maestro program [33] was employed for visualization, and all computations were carried out using the Schrödinger Materials Science Suite 2022-2.

Results and Discussion

The synthesized metal complexes remained stable at ambient conditions, dissolving in 1% DMSO, while the ligand itself was soluble in methanol. The complexes were also found to be soluble in DMF. According to the elemental analysis results, the metal complexes were formed in two distinct ratios: 1:2 (metal: 2HBMF) and 1:1:1 (metal: HBMF: 1,10-phen) [34]. The proposed molecular structures of the complexes are shown in **Figure 1.**
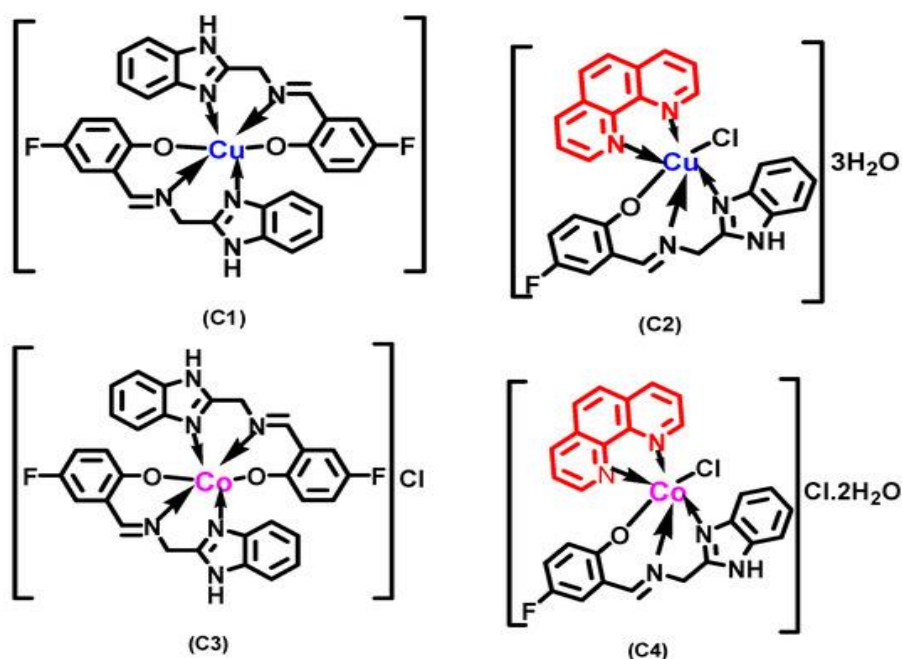

Figure 1. Predicted Structures of Metal Complexes (C1–C4).

UV-visible spectroscopic analysis

A subtle absorption feature in the 305–330 nm range corresponds to the azomethine bond. In particular, complexes C3 and C4 exhibited an absorption peak at 650 nm, indicative of the 1A1g→1T2g transition [34, 35]. A universal absorption band, seen between 390 and 435 nm across all complexes, points to possible charge transfer transitions. The electronic spectra of C1 and C2 suggested a distorted octahedral configuration, demonstrated by the absorption peak at 455 nm, which is linked to the 2B1g→2Eg transition. Additionally, the inclusion of the co-ligand 1,10-phenanthroline in C2 and C4 led to an additional band at 360 nm, which is attributed to the n→π* transition [36].

Infrared (IR) spectral analysis

In the FT-IR spectrum of HBMF, a medium-intensity band was detected at 1730 cm−1, characteristic of the C=N stretching in the benzimidazole ring. Another peak at 1638 cm−1 indicated the free azomethine group in the Schiff base ligand. However, in the metal complexes, this band shifted to a lower wavenumber, confirming that the azomethine nitrogen is coordinating with the metal ion [37]. A phenolic C-O stretching band appeared at 1270 cm−1 in HBMF, which shifted downward by 8–12 cm−1 in the metal complexes. This suggests that the phenolic –OH group is also involved in coordination with the metal centers [38].

Thermogravimetric behavior

Thermal analysis of the metal complexes was conducted over a temperature range from 27 to 800 °C, under an inert atmosphere and with a heating rate of 10 °C/min. The decomposition patterns of C1 and C3 were similar, with three distinct stages of weight loss [39]. As illustrated in **Figure 2**, C3 underwent an initial weight loss of 8.4% (calculated 8.2%) between 130–210 °C, corresponding to the departure of a chloride ion. At 270–390 °C, a further weight loss of 38.96% (calculated 37.12%) occurred due to the loss of two 5-fluorosalicyladihyde molecules. A significant mass loss of 45.43% (calculated 45.45%) was observed between 440–490 °C, attributed to the release of two aminomethylbenzimidazole molecules. The final residue was Co2O3.
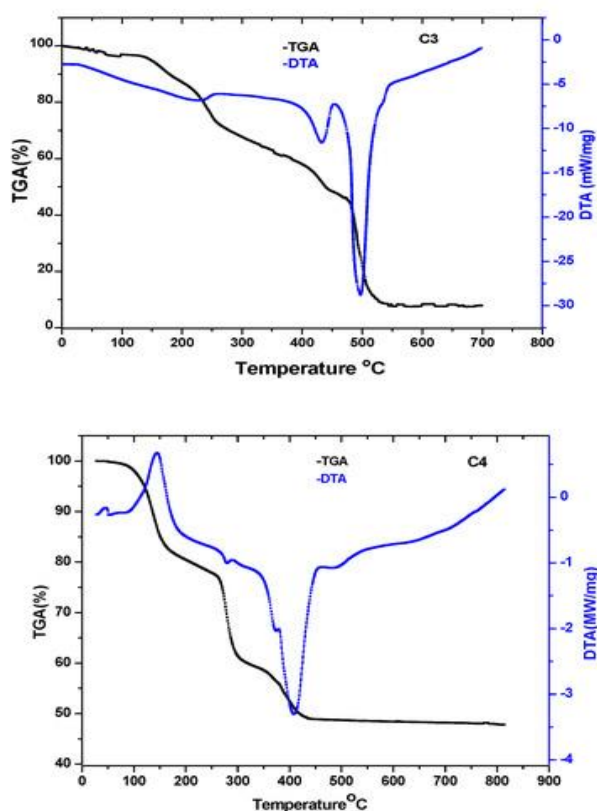

Figure 2. Thermal Decomposition and Differential Thermal Analysis of Complexes C3 and C4

The degradation patterns of complexes C2 and C4 showed similar thermal behavior. Several phases of weight loss were observed, indicating the instability of the compounds at high temperatures. Initially, water molecules and chloride ions were expelled from the complexes between 78–230 °C, resulting in an 8.91% weight loss, which matched the theoretical prediction. The next stage saw a significant 30.43% weight loss (theoretical: 30.23%) due to the removal of 1,10-phenanthroline between 265–330 °C. A further decomposition phase was observed from 390–470 °C, where 5-fluorosalicyladihyde was eliminated, accounting for a weight loss of 19.35% (calculated: 20.16%). The final weight reduction occurred from 490–520 °C, with 24.35% loss (theoretical: 24.69%) attributed to the departure of aminomethylbenzimidazole. After 540 °C, the complexes stabilized, indicating the formation of metal oxides.

Conductance and magnetic behavior

The molar conductance of the metal complexes (C1–C4) was assessed in DMSO, and the results revealed stable conductance over time, signifying that the complexes remain stable in solution. The complexes containing chloride ions (C3 and C4) displayed higher conductance compared to C1 and C2, confirming the presence of chloride outside the coordination sphere in the former complexes. The conductance values of Co(III) and Cu(II) complexes were 134 µS and 154 µS, respectively, at 25 °C, with the decrease in conductance attributed to the formation of the complexes.

Magnetic studies showed that the Cu(II) complex exhibited a magnetic moment of 1.87–1.89 BM, consistent with an octahedral geometry. The Co(III) complexes, in contrast, were diamagnetic, indicating a low-spin octahedral structure, which is typical for Co(III) complexes with a d6 electron configuration [40].

Mass spectrometry

The spectrum of C1 revealed a peak at m/z = 600.1157, which corresponds to the calculated value (600.0774). Similarly, C2 exhibited a peak at m/z = 600.1157 (M+) and a value of 601.51590, indicating the presence of water in the structure, in good agreement with the IR spectra [41]. C3 showed a molecular ion peak at m/z = 630.48, along with a [M-Cl]+ peak at m/z = 595.46. For C4, the molecular ion was observed at m/z = 614.1064, matching the calculated value (614.34082), consistent with the formation of a mixed-ligand complex.

Electron spin resonance (ESR)

The ESR spectra of the Cu(II) complexes, C1 and C2, were recorded at liquid nitrogen temperatures and analyzed for paramagnetic behavior. The spectra of C2 exhibited a dominant peak with weak additional peaks, indicating weak coupling of the unpaired electron to the copper nuclei, and suggesting electron delocalization towards the oxygen atoms. In contrast, C1's spectrum showed several peaks, indicating stronger delocalization of the unpaired electron through the nitrogen atom in the benzimidazole and azomethine groups due to super-hyperfine coupling interactions [42]. The ESR analysis showed g∥ and g⊥ values in the range of 2.343–2.191 and 2.070–2.066, respectively (**Table 1**), supporting the distorted octahedral coordination of Cu(II). The g⊥ and g∥ values indicated that the unpaired electron predominantly resides in the Cu(II) ion's dx2-y2 orbital (g⊥ > 2.0023), and the exchange coupling constant was calculated as G = (g∥ − 2.0023) / (g⊥ − 2.0023) [44].

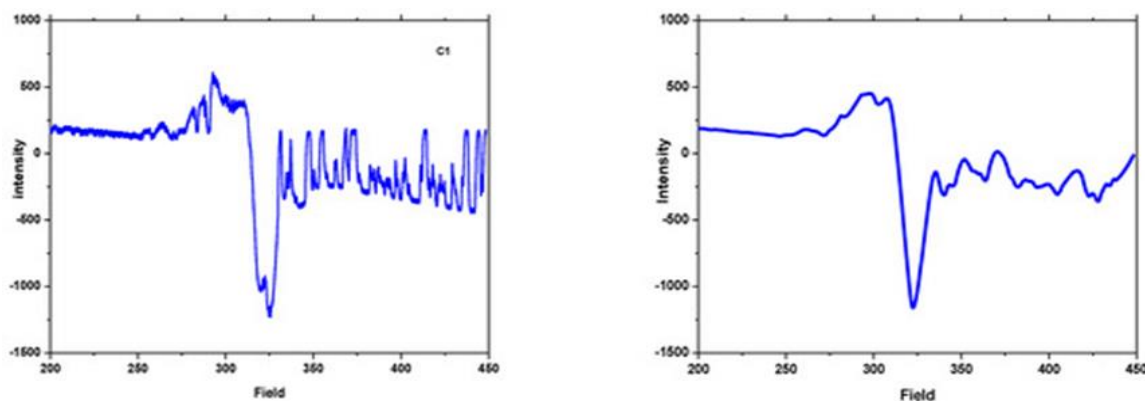**Figure 3.** ESR Spectra of Complexes C2 (left) and C1 (right).

Table 1. ESR Parameters (g∥ and g⊥) and Bonding Data for Complexes C1 and C2

Complexes	g∥	g⊥	G	g_{avg}	α^2	A∥	f = g∥/A∥
C2	2.1591	2.0332	3.7510	2.0751	0.67	171	126
C1	2.0708	2.0243	3.5822	2.0398	0.72	154	134

g∥—gyromagnetic ratio (parallel), g⊥—gyromagnetic ratio (perpendicular), G—Lande splitting factor, g_{avg}—gyromagnetic ratio (average), α—Spin states (spin population), A—Hyperfine coupling constant.

Biology

Pharmacological analysis

Cytotoxicity and Activity Relationship

The integration of metal ions with benzimidazole derivatives has attracted significant attention for the design of anticancer agents. Studies have demonstrated that benzimidazole-based complexes, such as salen derivatives, can effectively inhibit cell growth in various cancer types [44, 45]. In this study, the novel metal complexes with benzimidazole and phenanthroline were assessed for their cytotoxic and anti-proliferative activities using the EAC cell line as the primary model. Among all the compounds tested, complex C4, which incorporates a benzimidazole unit with a fluorine atom and 1,10-phenanthroline as a coordinating ligand, exhibited remarkable anti-cancer activity. It showed an IC50 value of 10 µM in the MTT assay, marking it as the most potent inhibitor of cell proliferation [46]. The effectiveness of C4 was further confirmed through in vivo studies aimed at evaluating its ability to restrict cell growth **(Figure 4).**
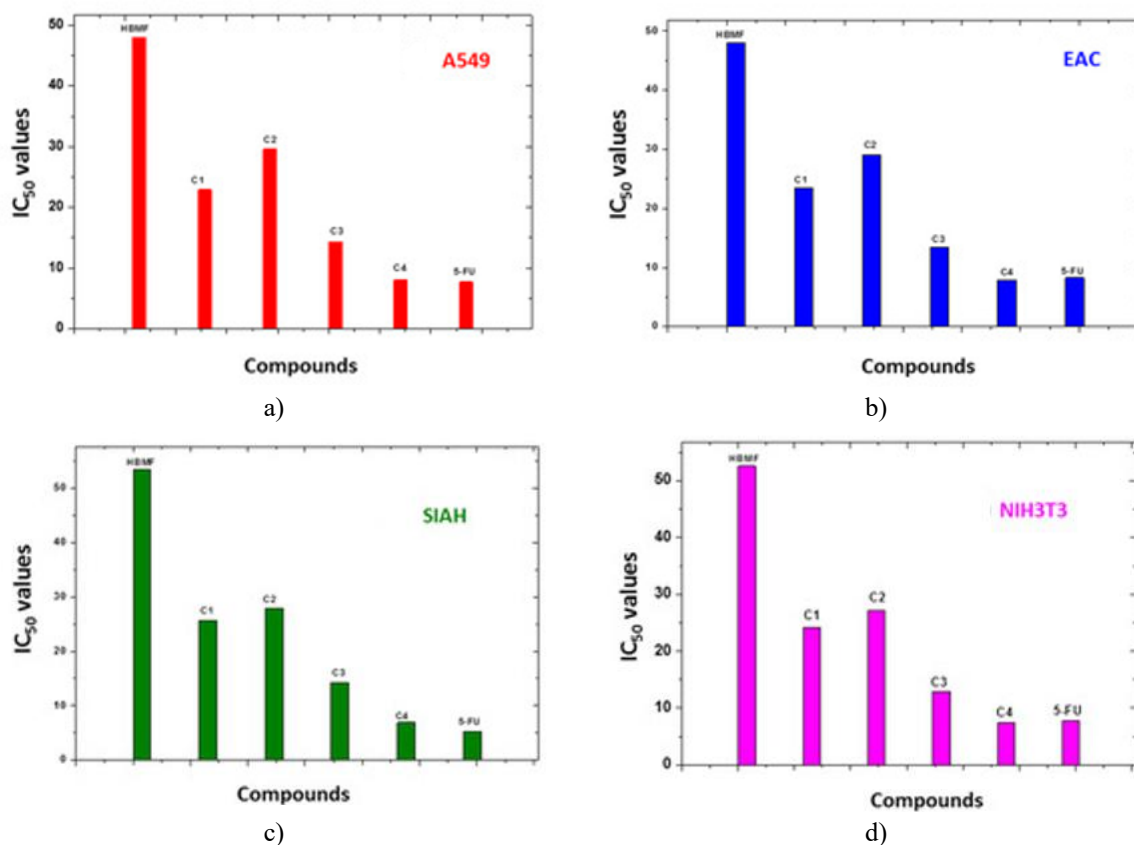

Figure 4. Screening of HMBF and its Complexes (C1–C4) for Cytotoxicity and Proliferation Inhibition
The cytotoxic effects and anti-proliferative activities of HMBF and its associated metal complexes (C1–C4) were evaluated against various cell lines: (a) A549, (b) EAC, (c) SIHA, and (d) NIH3T3. The IC50 values for each complex across these lines are presented.

Impact of complex C4 on hematological and serum parameters in EAC-bearing mice

Following a 20-day treatment with complex C4 at a dosage of 10 mg/kg in EAC cell-bearing mice, distinct alterations in the hematological profiles were recorded. The WBC count was significantly elevated in the EAC control group, while there was a decrease in alkaline phosphatase and urea concentrations in the EAC group. After

treatment with complex C4, these parameters showed significant recovery toward normal levels by day 25. The number of EAC cells was reduced by about 48.36% with the 10 mg/kg dose. Treatment with complex C4 also caused a slight increase in the number of macrophages and peritoneal cells in normal mice.
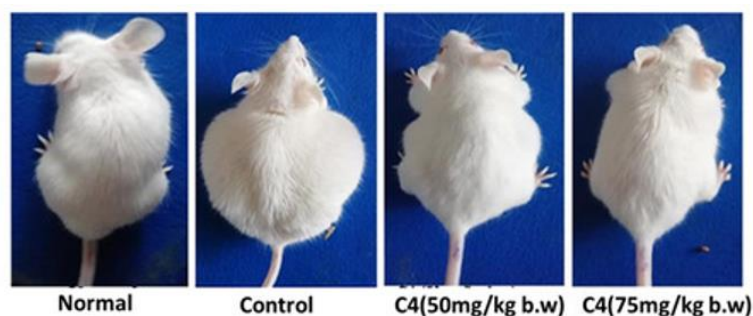
Table 2. Hematological and Serum Parameters for Normal and EAC-Bearing Mice Treated with C4 Complex (10 mg/kg)

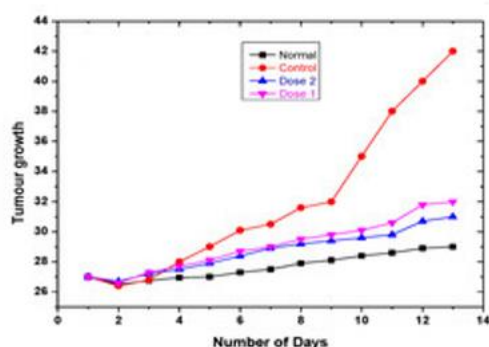| Parameter	Normal Mice	Treated Mice
Alkaline Phosphatase (IU/L)	136.78 ± 1.30	134.45 ± 2.1
Creatinine (mg/dL)	0.39 ± 1.3	0.43 ± 1.25
Urea (mg/dL)	48 ± 2.2	43 ± 2.3
RBC (106/μL)	5.7 ± 0.5	5.4 ± 0.6
WBC (106/μL)	3.56 ± 2.3	3.5 ± 2.4

Complex C4 Inhibits EAC Tumor Cell Proliferation

The fundamental features of cancer, such as evasion of apoptosis, uncontrolled growth, and angiogenesis, are common across various cancer types. A primary goal of anticancer drugs is to target and inhibit these hallmarks [47]. When the EAC cell line was introduced into healthy mice, it triggered a local inflammatory response, which increased vascular permeability, leading to cellular migration and significant ascites fluid accumulation. Cancer cells rely on this fluid for essential nutrients required for growth, so limiting ascites formation can effectively halt tumor growth [48-50].
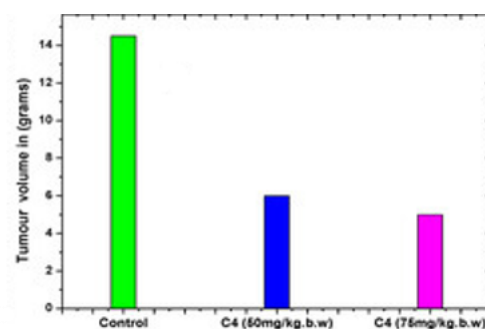
In this study, complex C4, the active compound, was administered intraperitoneally (i.p.) at doses of 50 and 75 mg per kg of body weight, as determined by LD50 studies. Complex C4 demonstrated substantial inhibition of tumor growth and a reduction in tumor size starting from the fifth day of treatment, as shown in the physical appearance and tumor volume data in **Figures 5a–5c**. The tumor inhibitory effects were more pronounced with increasing dosages, as observed in the pharmacological assays. Furthermore, treatment with complex C4 led to a decrease in ascites fluid and tumor cell count (**Figures 5d and 5e).** Compared to the control group, the survival rate of the treated mice was significantly higher—approximately two times greater—between days 12 and 26 (**Figure 5f)** [51]. Acute toxicity studies also revealed that the internal organs of the treated mice were nearly unaffected, in contrast to the untreated group, which exhibited enlarged spleens and livers, further confirming the effectiveness of complex C4 in inhibiting cell proliferation.

a)

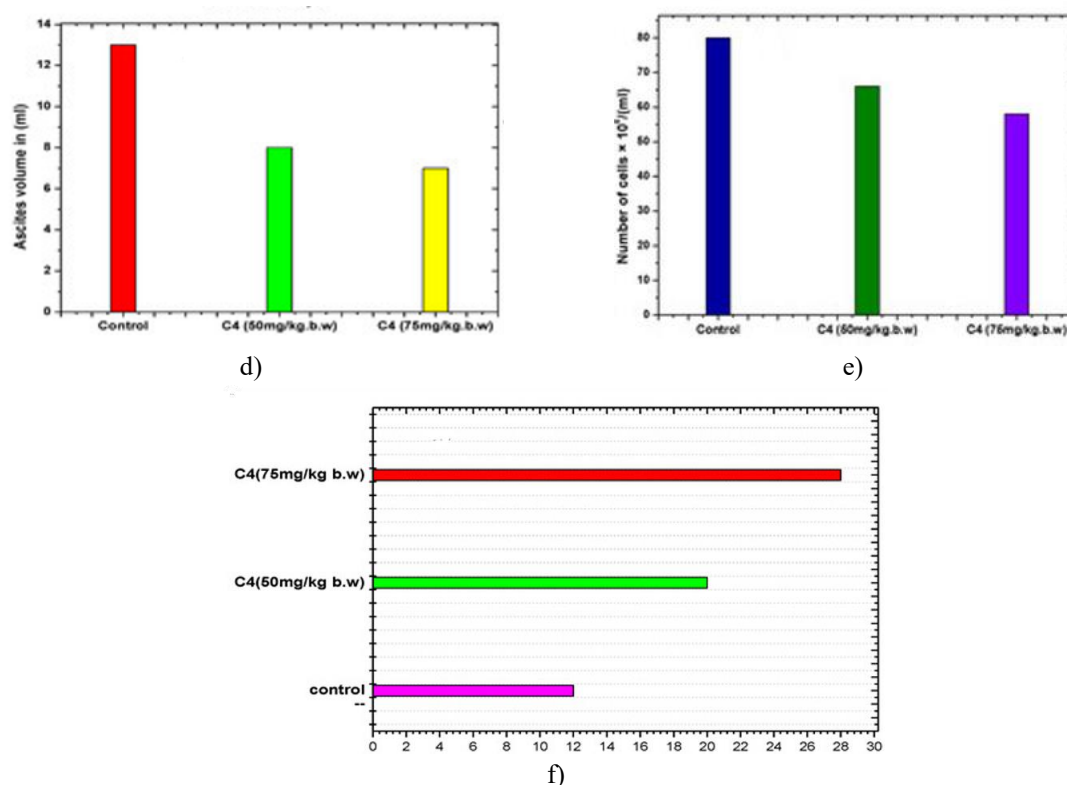b)   c)

d)

e)

f)

Figure 5. The Impact of Complex C4 on Ehrlich Ascites Carcinoma (EAC) in Mice
EAC cells were injected intraperitoneally, leading to the development of ascitic tumors in one-and-a-half-month-old Swiss albino mice. Two doses of complex C4 (50 mg/kg and 75 mg/kg) were administered to the tumor-bearing mice every alternate day, starting three days after tumor growth. The following results were observed:
(a) Tumor morphology in the mice, (b) Reduced tumor volume, (c) Tumor volume in grams, (d) Decrease in ascites secretion, (e) Reduction in tumor cell proliferation, comparing treated versus control groups, (f) Kaplan-Meier survival analysis showing prolonged survival in treated mice.

Angiogenesis

The balance between slow cellular apoptosis and rapid angiogenesis plays a crucial role in regulating cell proliferation. Angiogenesis is the complex process of forming new blood vessels from pre-existing ones [52]. Neovascularization is essential in wound healing, embryonic development, and inflammation, primarily regulated by vascular endothelial growth factor (VEGF). When VEGF is over-activated, angiogenesis accelerates, recruiting inflammatory cells that contribute to tumor formation. Suppressing angiogenesis—by blocking VEGF—can inhibit tumor growth by inducing cellular apoptosis, leading to cell death and halting tumor expansion [53].

Angiogenesis controls both tumor growth and metastasis, which is evident in many in vivo studies. The growth of tumors and their spread via blood vessels is primarily driven by increased neovascularization. By blocking angiogenesis, tumor growth can be arrested and metastasis can be reduced. Numerous studies have shown that tumors with extensive vascularization tend to have poorer survival rates, while those with less vasculature correlate with better survival outcomes. The extent of neovascularization or microvessel density (MVD) is commonly used to assess disease prognosis. In this study, the EAC cell line, which serves as a convenient model for MVD analysis, was utilized to observe the effects of complex C4.

Key angiogenic assays, including the CAM and H&E staining methods, were performed to evaluate complex C4's impact on MVD. The results indicated that complex C4 significantly reduced the vascular supply, as observed in both peritoneal angiogenesis and CAM assays **(Figures 6a and 6b).** The reduction in neovascularization, observed through H&E staining, strongly supports the anti-angiogenic properties of complex C4 **(Figure 6c).**
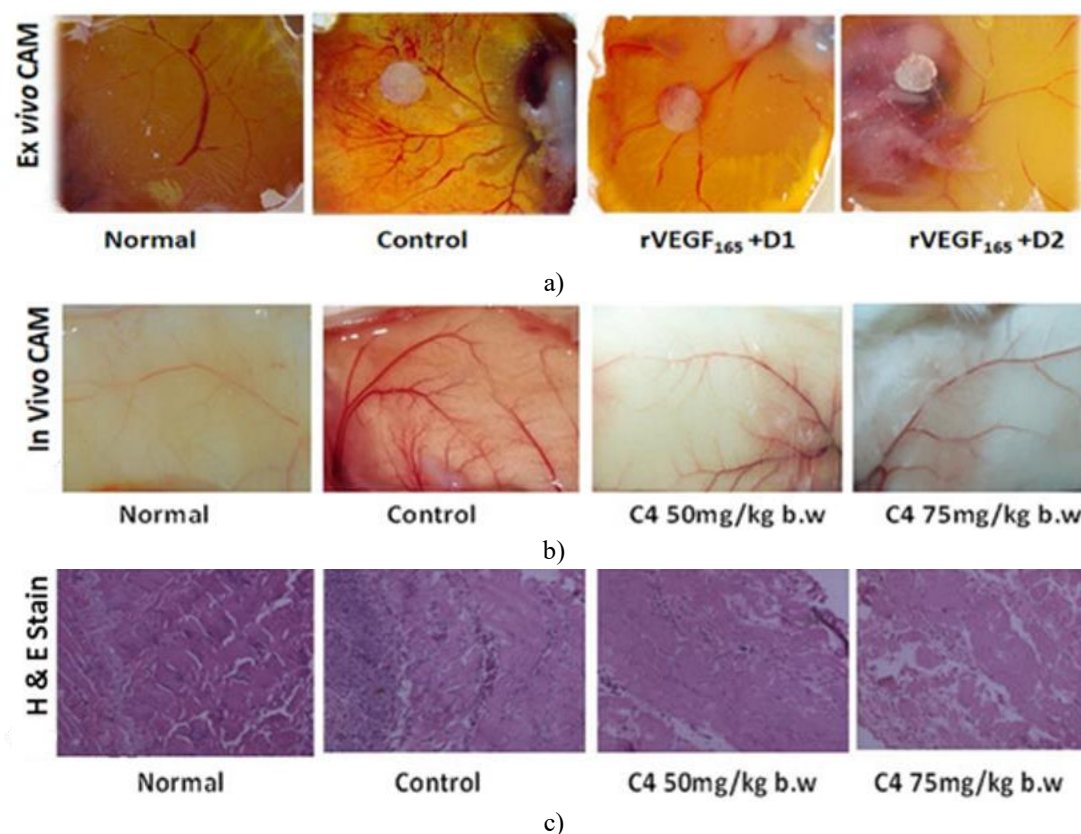
Figure 6. Complex C4 Impacts Microvascular Formation in Non-Tumor Models
The effect of complex C4 on angiogenesis was assessed by promoting blood vessel formation using rVEGF165 in non-tumor models, followed by treatment with complex C4. (a) Ex vivo and (b) In vivo images from the CAM assay reveal a noticeable reduction in neovascularization upon treatment with complex C4. (c) Hematoxylin and eosin staining of peritoneal tissue sections shows a substantial decrease in vascular density, confirming the anti-angiogenic effect of complex C4.

Computational findings
  Local reactivity of the ligand
The local reactivity of the molecular structures under study was examined by analyzing the frontier molecular orbitals (FMOs) and other quantum descriptors. These calculations were carried out using the DFT method at the M06-2X/LACVP (d,p) level. FMOs are vital for understanding a molecule's reactivity: the HOMO is electron-rich, while the LUMO represents sites that accept electrons. The energy gap between these orbitals provides insight into the molecule's stability and reactivity, while their spatial distribution highlights the regions most likely to interact [53].

For a deeper understanding, the molecular electrostatic potential (MEP) and the average local ionization energy (ALIE) were also assessed. MEP identifies regions prone to non-covalent interactions, whereas ALIE helps pinpoint areas susceptible to electrophilic attacks. These reactivity descriptors were mapped onto the molecule's electron density surfaces, as illustrated in **Figure 7**. The surfaces for FMOs, MEP, and ALIE of the HBMF molecule are shown to highlight areas of high reactivity.
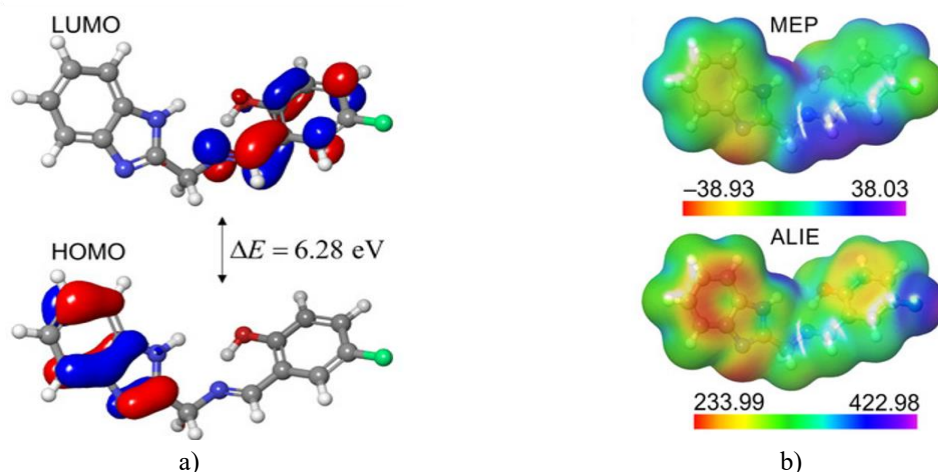
Figure 7. (a) Frontier Molecular Orbitals (FMOs) and (b) Molecular Electrostatic Potential (MEP) and Average Local Ionization Energy (ALIE) Surfaces of the HBMF Molecule.

The maximum and minimum MEP and ALIE values are expressed in kcal/mol. Surfaces were derived using isovalues of ±0.050 a.u. for FMOs and ±0.001 a.u. for MEP/ALIE [54, 55]. The FMO results shown in **Figure 7a** reveal a well-separated HOMO and LUMO for the HBMF molecule. The HOMO is primarily spread across the region where the benzene ring is fused with the imidazole group, indicating this part of the molecule is electron-rich and capable of donating electrons. In contrast, the LUMO is distributed over the second benzene ring and the bridging chain, areas that are electron-deficient and tend to accept electrons. The significant gap between the HOMO and LUMO (6.28 eV) suggests that the HBMF molecule is quite stable, with substantial charge transfer occurring between its components upon excitation.

The MEP surface in **Figure 7b** identifies two primary reactive sites on the HBMF molecule. The lowest MEP value (−38.93 kcal/mol) is located near the nitrogen atom in the imidazole group, indicating a region that is prone to interaction with positively charged fragments. Conversely, the highest MEP value (38.03 kcal/mol) is near the hydrogen atom connected to another nitrogen in the imidazole group, suggesting this region is reactive towards negatively charged species. Similarly, the ALIE surface shows the lowest and highest ALIE values near these same regions. The ALIE descriptor highlights the nitrogen atom of the imidazole as highly susceptible to electrophilic attacks, while the area near the fused benzene ring also exhibits vulnerability to such attacks.

Interaction of HBMF with water

Understanding how HBMF interacts with water molecules is crucial for evaluating its biological relevance [54]. To explore this, we conducted molecular dynamics (MD) simulations of the HBMF molecule in a water environment, surrounded by approximately 2000 water molecules. After 10 ns of simulation, we analyzed the radial distribution functions (RDFs) to examine the reactivity of the HBMF atoms with water molecules. The RDFs, which show the relationship between the distance of HBMF atoms and the oxygen atoms of the surrounding water, are illustrated in **Figure 8.**
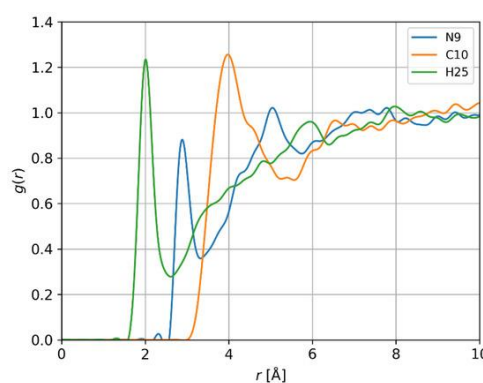

Figure 8. RDFs Representing the Interaction of HBMF Molecule with Water**.**

In **Figure 8**, the radial distribution function (RDF) results highlight that the HBMF molecule exhibits strong interactions with water molecules through a single atom. This key atom is the hydrogen (H25), which is attached to the nitrogen in the imidazole fragment. This hydrogen atom corresponds to the highest MEP values, as shown in **Figure 7b**. The RDF for this atom reveals a prominent peak at a distance of approximately 2 Å, suggesting a strong attraction between H25 and the surrounding water molecules.

Further analysis shows that two additional atoms, nitrogen (N9) and carbon (C10), also interact with water, but to a lesser degree. The nitrogen atom (N9) produces a sharp peak in the RDF around 3 Å, indicating moderate interaction. The RDF for the carbon atom (C10) shows a peak at about 4 Å, which suggests a weaker interaction with water.
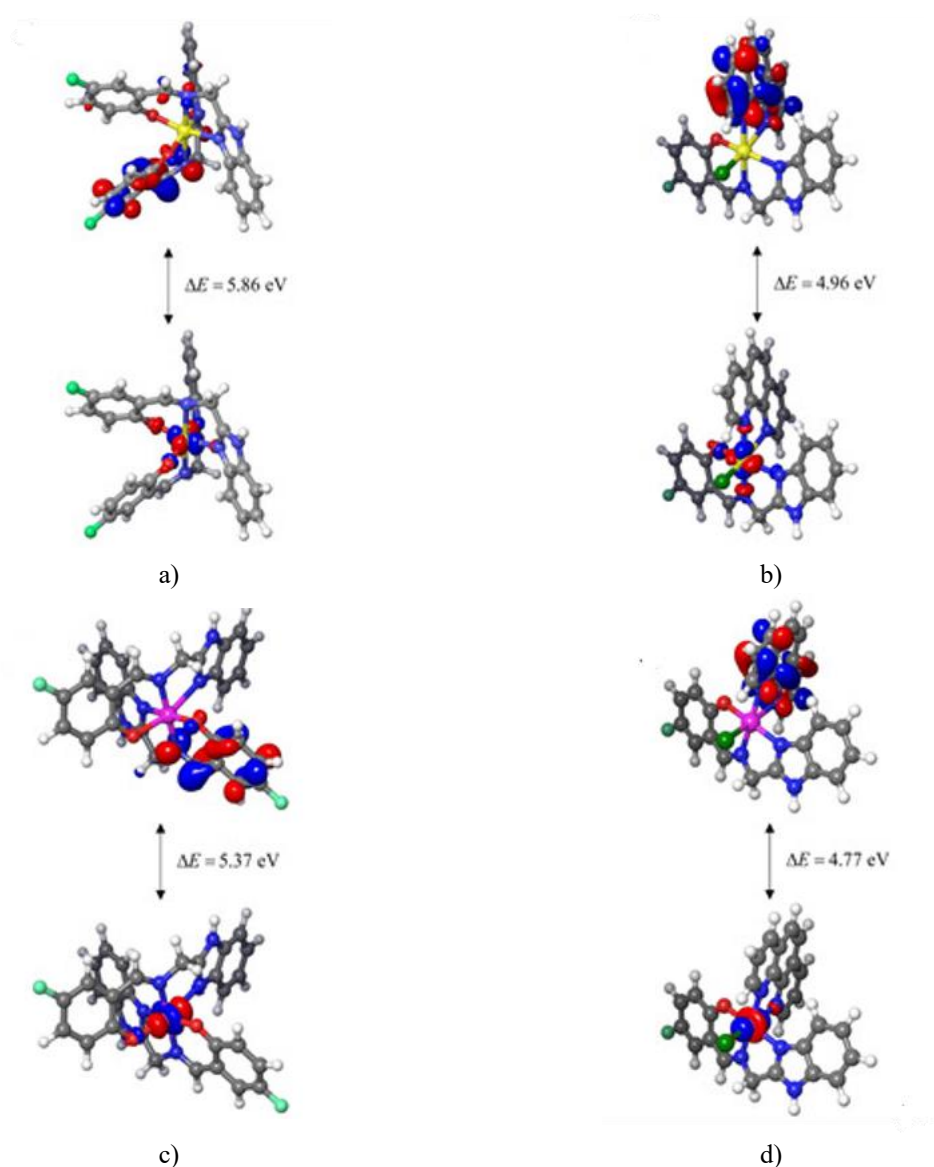

Figure 9. Frontier Orbitals of Complexes C1 to C4

The diagram illustrates the frontier molecular orbitals (FMOs) for the complexes: (a) C1, (b) C2, (c) C3, and (d) C4, showing their respective energy gaps between the highest occupied molecular orbital (HOMO) and lowest unoccupied molecular orbital (LUMO). These surfaces are depicted using isovalues of ±0.050 a.u.

Analysis of reactivity in the metal complexes

To assess the reactivity of the complexes, single-point energy calculations were carried out at the same theoretical level. This provided insights into the FMOs, molecular electrostatic potential (MEP), and average local ionization energy (ALIE) distributions. The FMOs for the complexes are presented in **Figure 10**, while their MEP and ALIE surfaces are shown in **Figure 11**.
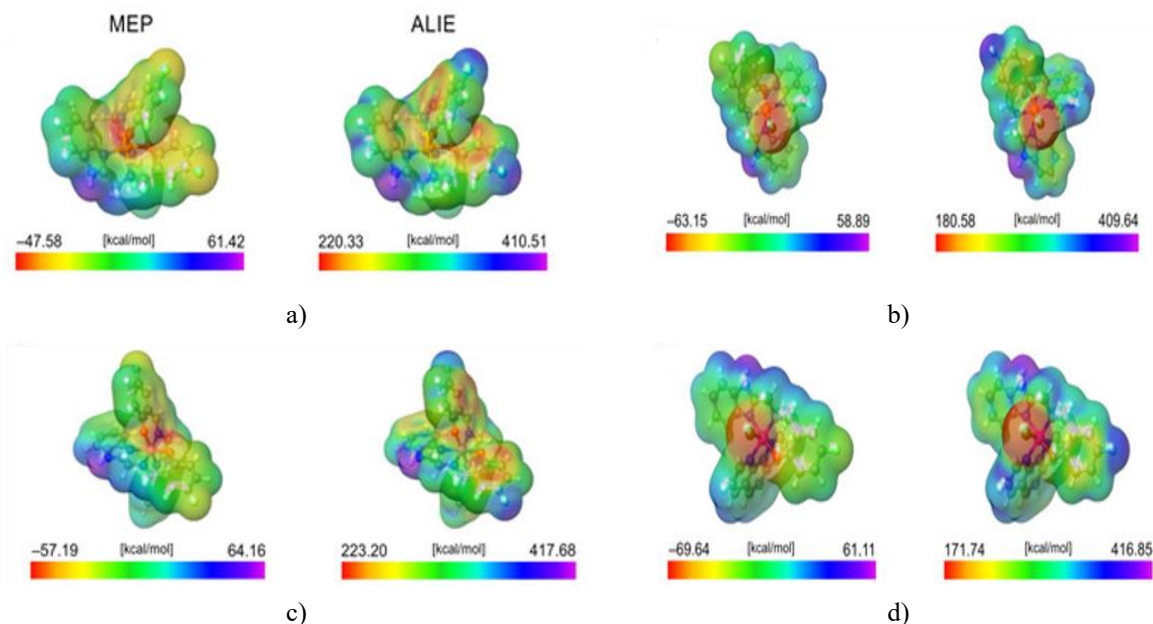
Figure 10. Panels (a–d) display the molecular electrostatic potential (MEP) and average local ionization energy (ALIE) surfaces for the complexes C1, C2, C3, and C4. The surfaces are represented by isovalues of ±0.001 a.u.
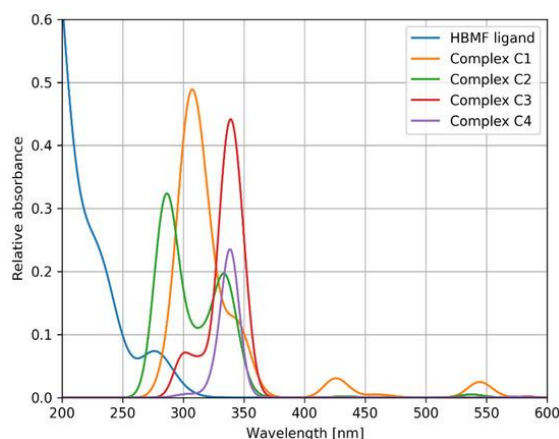

Figure 11. Simulated UV Absorption Spectra of the Studied Complexes.

The findings associated with the ΔE values presented in **Figure 9** reveal that the most stable complex is C1, with a corresponding energy gap of 5.86 eV. This is followed by complexes C3 (5.36 eV) and C2 (4.96 eV), while the least stable complex is C4 with a gap of 4.77 eV. For all complexes, the HOMO is localized around the metal site, while the LUMO is confined to a single fragment of the molecule.

According to the MEP data, complex C4 is the most reactive towards positively charged entities, exhibiting the lowest MEP value of −69.64 kcal/mol near its chlorine atom. In terms of reactivity, C4 is followed by C2, C3, and C1 with MEP values of −63.15, −57.19, and −47.58 kcal/mol, respectively. Conversely, complex C3 is the most reactive towards negatively charged species, with its highest MEP value recorded at 64.16 kcal/mol, followed by C1, C4, and C2.

The distribution of ALIE values mirrors that of the MEP values but also reveals significant differences in susceptibility to electrophilic attacks. The lowest ALIE values for C4 and C2 are 40-50 kcal/mol lower than those for C1 and C3, indicating a stark contrast in their reactivity. Complex C4 once again emerges as the most reactive in terms of electrophilic attack.

Simulated UV spectra analysis

TD-DFT was utilized to simulate the UV absorption spectra for all the complexes. A long-range corrected version of the B3LYP functional, CAM-B3LYP, was employed, using the LACVP+(d,p) basis set. For the excitation analysis, the Tam-Dancoff approximation was applied due to the complexity of the structures. The simulated UV spectra are presented in **Figure 11.**

When compared to experimental data, HBMF exhibited a peak absorption around 300 nm, though the calculated spectrum placed it closer to 275 nm. The match between experimental and simulated spectra is excellent for complexes C1 and C2, both showing two distinct peaks. However, there was a slight discrepancy in their wavelengths, likely due to the approximation used in the TD-DFT calculations. The agreement between theory and experiment for complexes C3 and C4 was not as strong, as the second absorption peak near 400 nm was not fully captured, though a good overall agreement was still achieved.

Conclusion

We have successfully synthesized and characterized a series of novel mononuclear benzimidazole-based saline complexes, namely [Cu(HBMF)2], [Cu(HBMF)(phen)Cl]3H2O, [Co(HBMF)2]Cl, and [Co(HBMF)(phen)Cl]Cl·2H2O. The experimental data confirm the proposed molecular structures, coordination modes, and geometries. The complexes exhibit strong thermal stability, as demonstrated by TGA/DTA analysis. Computational studies of the ligand showed well-separated FMOs, indicating high stability, with a significant energy gap (ΔE). According to combined MEP and ALIE descriptors, complex C4 shows the highest reactivity. MD simulations revealed that the hydrogen atom H25 in the imidazole fragment interacts most strongly with water molecules. The UV spectra simulation showed good agreement with experimental results. Additionally, the pharmacological properties of the complexes were assessed via in vitro and in vivo anti-proliferative assays and anti-angiogenesis studies. Among the complexes, C4 stood out as the most potent compound, exhibiting remarkable tumor-suppressing capabilities with minimal toxicity. Complex C4 was also found to accelerate apoptosis by hindering neovascularization, as evidenced by the anti-angiogenesis assay. Nuclear fragmentation, a hallmark of cellular apoptosis, was prominently observed.

Acknowledgments: None

Conflict of Interest: None

Financial Support: None

Ethics Statement: None

References

1. Ndagi, U.; Mhlongo, N.; Soliman, E. Metal complexes in cancer therapy an update from drug design perspective. Drug Des. Dev. Ther. 2017, 11, 599–616.
2. Dasari, S.; Tchounwon, P. Cisplatin in cancer therapy: Molecular mechanism of action. Eur. J. Pharmacol. 2014, 740, 364–378.
3. Alam, R.; Wahi, D.; Singh, R.; Sinha, D.; Tandon, V.; Grover, A.; Rahisuddin. Design, synthesis, cytotoxicity, HuTopoIIαinbitory activity and molecular docking studies of pyrazolederivatives as potential anticancer agents. Bioorg. Chem. 2016, 69, 77–90.
4. Vasamthakumar, B.C.; Lohith, G.K.; Revanasiddappa, H.D. Co(III) and Cu(II) Benzimidazole base complexes: Synthesis, Characterization and DNA binding and cleavage activity. J. Chem. Biol. Phys. Sci. 2017, 7, 882–895.
5. Song, W.-J.; Cheng, J.-P.; Jiang, D.-H.; Guo, L.; Cai, M.-F.; Yang, H.-B.; Lin, Q.-Y. Synthesis, interaction with DNAand antiproliferative activities of two novel Cu(II) complexes with Schiff base of benzimidazole. Spectrochim. A Mol. Biomol. Spectrosc. 2014, 121, 70–76.
6. Sunitha, M.; Jogi, P.; Ushaiah, B.; Gayanakumari, C. Synthesis, Characterization and Antimicrobial activity of transition metal complexes of Schiff base ligand derived from 3- ethoxy salicylaldehyde and 2-(2-aminophenyl) 1-H-benzimidazole. E-J. Chem. 2012, 9, 2516–2523.

7. Savithri, K.; Vasantha kumar, B.V.; Vivek, H.K.; Revanasiddappa, H.D. Synthesis and Characterization of Cobalt(III) and Copper(II) Complexes of 2-((E)-(6-Fluorobenzo[d]thiazol-2-ylimino) methyl)-4-chlorophenol: DNA Binding and Nuclease Studies—SOD and Antimicrobial Activities. Int. J. Spectrosc. 2018, 2018, 8759372.

8. Esteghamat-Panah, R.; Farrokhpour, H.; Hadadzadeh, H.; Abyar, F.; Rudbari, H.A. An experimental and quantum chemical study on the non-covalent interactions of a cyclometallated Rh(III) complex with DNA and BSA. RSC Adv. 2016, 6, 23913–23929.

9. Rajarajeswari, C.; Loganathan, R.; Palaniandavar, M.; Suresh, E.; Riyasdeend, A.; Abdulkadhar, M. Copper(II) complexes with 2NO and 3N donor ligands: Synthesis, structures and chemical nuclease and anticancer activities. Dalton Trans. 2013, 42, 8347–8363.

10. Wright, J.B. Structure and antioxidant superoxide dismutase. Chem. Rev. 1951, 48, 397–541.

11. Paularokiadoss, F.T.; Christopher Jeyakumar, R.; Thomas, A.; Sekar, D.; Bhakiaraj. Group 13 monohalides [AX (A = B, Al, Ga and In; X = Halogens)] as alternative ligands for carbonyl in organometallics: Electronic structure and bonding analysis. Comput. Theor. Chem. 2022, 1209, 113587.

12. Stanojev, J.S.; Armakovic, B.; Bajac, J.; Matovic, V.; Srdic, V. PbSe sensitized with iodine and oxygen: A combined computational and experimental study. J. Alloys Compd. 2022, 896, 163119.

13. Al-Otaibi, J.S.; Mary, Y.S.; Ullah, Z.; Kwon, H.W. Adsorption behavior and solvent effects of an adamantane-triazole derivative on metal clusters—DFT simulation studies. J. Mol. Liq. 2022, 345, 118242.

14. Reichert, T.; Vučićević, M.; Hillman, P.; Bleicher, M.; Armaković, S.S.; Armaković, J. Sumanene as a delivery system for 5-fluorouracil drug—DFT, SAPT and MD study. J. Mol. Liq. 2021, 342, 117526.

15. Suntharalingam, K.; Mendoza, O.; Duarte, A.A.; Mann, D.J.; Vilar, R. A platinum complex that binds noncovalently to DNA and induces cell death via a different mechanism than cisplatin. Metallomics 2013, 5, 514–523.

16. Kumaravel, G.; Ponya Utthra, P.; Raman, N. Exploiting the biological efficacy of benzimidazole based Schiff base complexes with l-Histidine as a co-ligand: Combined molecular docking, DNA interaction, antimicrobial and cytotoxic studies. Bioorg. Chem. 2018, 77, 269–279.

17. Schildkraut, C.L.; Marmur, J.; Doty, P. The formation of hybrid DNA molecules and their use in studies of DNA homologies. J. Mol. Biol. 1961, 3, 595–617.

18. Krishnamurthy, G.; Shashikal, J. Complexes of zinc(II) with 1,2-disubstituted benzimidazoles. J. Chem. Res. 2006, 14, 766–768.

19. Prabhakar, B.T.; Ara Khanum, S.; Jayashree, K.; Bharathi, P.; Shashikanthc, S. Anti-tumor and proapoptotic effect of novel synthetic benzophenone analogues in Ehrlich ascites tumor cells. Bioorg. Med. Chem. 2006, 14, 435–446.

20. Danihelová, M.; Veverka, M.; Sturdík, E.; Jantová, S. Antioxidant action and cytotoxicity on HeLa and NIH-3T3 cells of new quercetin derivatives. Toxicology 2013, 6, 209–216.

21. MacroModel Schrödinger Release 2022-1: MacroModel; Schrödinger LLC: New York, NY, USA, 2022.

22. Becke, A.D. Density-functional thermochemistry. III. The role of exact exchange. J. Chem. Phys. 1993, 98, 5648–5652.

23. Rassolov, V.A.; Ratner, M.A.; Pople, J.A.; Redfern, P.C.; Curtiss, L.A. 6-31G* basis set for third-row atoms. J. Comput. Chem. 2001, 22, 976–984.

24. Bannwarth, C.E.; Caldeweyher, S.; Ehlert, A.; Hansen, P.; Pracht, J.; Seibert, S.; Spicher, S.; Grimme, E. Extended tight-binding quantum chemistry methods, Wiley Interdiscip. Rev. Comput. Mol. Sci. 2021, 11, e1493.

25. Thompson, J.D.; Winget, P.; Truhlar, D.G. MIDIX basis set for the lithium atom: Accurate geometries and atomic partial charges for lithium compounds with minimal computational cost. Phys. Chem. Commun. 2001, 4, 72–77.

26. Zhao, Y.; Truhlar, D.G. The M06 suite of density functionals for main group thermochemistry, thermochemical kinetics, noncovalent interactions, excited states, and transition elements: Two new functionals and systematic testing of four M06-class functionals and 12 other function. Theor. Chem. Acc. 2008, 120, 215–241.

27. Hay, P.J.; Wadt, W.R. Ab initio effective core potentials for molecular calculations. Potentials for K to Au including the outermost core orbitals. J. Chem. Phys. 1985, 82, 299.

28. Yanai, T.; Tew, D.P.; Handy, N.C. A new hybrid exchange–correlation functional using the Coulomb-attenuating method (CAM-B3LYP). Chem. Phys. Lett. 2004, 393, 51–57.

29. Harder, E.; Damm, W.; Maple, J.; Wu, C.; Reboul, M.; Xiang, J.Y.; Wang, L.; Lupyan, D.; Dahlgren, M.K.; Knight, J.L. OPLS3: A force field providing broad coverage of drug-like small molecules and proteins. J. Chem. Theory Comput. 2016, 12, 281–296.

30. Berendsen, H.J.C.; Postma, J.P.M.; van Gunsteren, W.F.; Hermans, J. Interaction Models for Water in Relation to Protein Hydration. In Intermolecular Forces; Springer: Berlin/Heidelberg, Germany, 1981; pp. 331–342.

31. Bochevarov, A.D.; Harder, E.; Hughes, T.F.; Greenwood, J.R.; Braden, D.A.; Philipp, D.M.; Rinaldo, D.; Halls, M.D.; Zhang, J.; Friesner, R.A. Jaguar: A high-performance quantum chemistry software program with strengths in life and materials sciences. Int. J. Quantum Chem. 2013, 113, 2110–2142.

32. Jacobson, L.D.; Bochevarov, A.D.; Watson, M.A.; Hughes, T.F.; Rinaldo, D.; Ehrlich, S.; Steinbrecher, T.B.; Vaitheeswaran, S.; Philipp, D.M.; Halls, M.D. Automated transition state search and its application to diverse types of organic reactions. J. Chem. Theory Comput. 2017, 13, 5780–5797.

33. Schrödinger Release 2021-4: Desmond Molecular Dynamics System; D E. Shaw Research Maestro-Desmond Interoperability Tools; Schrödinger: New York, NY, USA, 2021.

34. Prakasha, G.; Shiva Prasad, K.; Syed, I.; Revanasiddappa, H.D. Novel Benzimidazole Derived Imine-Based Ligand and its Co(III), Ni(II), Cu(II) and Pt(II) Complexes: Chemical Synthesis, Structure, Antimicrobial, DNA Interaction Studies and Nuclease Activity. Lett. Appl. Nanobiosci. 2020, 9, 1655–1672.

35. Vijay Avin, B.R.; Thirusangu, P.; Lakshmi Ranganatha, V.; Firdouse, A.; Prabhakar, B.T.; Ara Khanum, S. Synthesis and tumor inhibitory activity of novel coumarin analogs targeting angiogenesis and apoptosis. Eur. J. Med. Chem. 2014, 75, 211–221.

36. Weidner, N.; Semple, J.P.; Welch, W.R.; Folkman, J. Tumor Angiogenesis and Metastasis—Correlation in Invasive Breast Carcinoma. N. Engl. J. Med. 1991, 324, 1–8.

37. Singh, Y.P.; Patel, R.N.; Singh, Y.; Butcher, R.J.; Vishakarma, P.K. Structure and antioxidant superoxide dismutase activity of copper(II) hydrazone complex. Polyhedron 2017, 122, 1–15.

38. Ommenya, F.K.; Nyawade, E.A.; Andala, D.M.; Kinyua, J. Synthesis, Characterization and Antibacterial Activity of Schiff Base, 4-Chloro-2-{(E)-[(4-Fluorophenyl)imino]methyl}phenol Metal (II) Complexes. J. Chem. 2020, 2020, 1745236.

39. Hussain, A.; Al Ajmi, F.M.; Rehman, T.; Amir, S.; Husain, M.; Alsalme, A.; Siddiqui, A.; Khan, A. Copper(II) complexes as potential anticancer and Nonsteroidal antiinfammatory agents: In vitro and in vivo studies. Sci. Rep. 2019, 9, 5237.

40. Chauhan, M.; Banerjee, K.; Arjmand, F. DNA Binding Studies of Novel Copper(II) Complexes Containing l-Tryptophan as Chiral Auxiliary: In Vitro Antitumor Activity of Cu−Sn2 Complex in Human Neuroblastoma Cells. Inorg. Chem. 2007, 46, 3072–3082.

41. Gurupadaswamy, H.D.; Girish, V.; Kavitha, C.V.; Raghavan, S.C.; Khanum, S.A. Synthesis and evaluation of 2,5-di(4-aryloylaryloxymethyl)- 1,3,4-oxadiazoles as anti-cancer agents. Eur. J. Med. Chem. 2013, 63, 536–543.

42. Fuh-An, Y.; Chih-Wei, G.; Yao-Jung, C.; Jyh-Horung, C.; Shin-Shin, W.; Jo-Yu, T.; Lian-Pin, H.; Shanmugam, E. ESR, zero-field splitting, and magnetic exchange of exchange-coupled copper(II)-copper(II) pairs in copper(II) tetraphenylporphyrin N-oxide. Inorg. Chem. 2007, 46, 578–585.

43. Thamilarasan, V.; Sengottuvelan, N.; Sudha, A.; Srinivasan, P.; Chakkaravarthi, G. Cobalt(III) complexes as potential anticancer agents: Physicochemical, structural, cytotoxic activity and DNA/protein interactions. Photochem. Photobiol. 2016, 162, 558–569.

44. Gupta, M.; Mazumder, U.K.; Kumar, R.S.; Sivakumar, T.; Vamsi, M.L.M. Antitumor Activity and Antioxidant Status of Caesalpinia bonducella Against Ehrlich Ascites Carcinoma in Swiss Albino Mice. J. Pharmacol. Sci. 2004, 94, 177–184.

45. Staton, C.A.; Reed, M.W.R.; Brown, N.J. A critical analysis of current in vitro and in vivo angiogenesis assays. Int. J. Exp. Pathol. 2008, 90, 195–221.

46. Hanahan, D.; Weinberg, R.A. Hallmarks of Cancer: The Next Generation. Cell 2011, 144, 646–674.

47. Folkman, J. Angiogenesis: An organizing principle for drug discovery. Nat. Rev. Drug Discov. 2007, 6, 273–286.

48. Kumar, S.N.; Krishnamurthy, G.; Yadav, D.; Malojirao, V.H.; Naik, R.T.R.; Kandagallae, S.; Prabhakar, B.T. Synthesis, characterization and tumor inhibitory activity of a novel Pd(II) complex derived from methanethiol-bridged (2-((1H-benzo[d]imidazol2-yl)methylthio)-1H-benzo[d]imidazol6-yl)(phenyl)methanon. New J. Chem. 2019, 43, 790–806.

49. Politzer, P.; Murray, J.S.; Bulat, F.A. Average local ionization energy: A review. J. Mol. Model. 2010, 16, 1731–1742.

50. Sjoberg, P.; Politzer, P. Use of the electrostatic potential at the molecular surface to interpret and predict nucleophilic processes. J. Phys. Chem. 1990, 94, 3959–3961.

51. Murray, J.S.; Politzer, P. The electrostatic potential: An overview. Wiley Interdiscip. Rev. Comput. Mol. Sci. 2011, 1, 153–163.

52. Politzer, P.; Murray, J.S. The average local ionization energy: Concepts and applications. Theor. Comput. Chem. 2007, 7, 119–137.

53. Grimme, S.; Bannwarth, C.; Shushkov, P. A Robust and Accurate Tight-Binding Quantum Chemical Method for Structures, Vibrational Frequencies, and Non-covalent Interactions of Large Molecular Systems Parametrized for All spd-Block Elements (Z = 1–86). J. Chem. Theory Comput. 2017, 13, 1989–2009.

54. Bannwarth, C.; Caldeweyher, E.; Ehlert, S.; Hansen, A.; Pracht, P.; Seibert, J.; Spicher, S.; Grimme, S. Extended tight-binding quantum chemistry methods, WIREs. Comput. Mol. Sci. 2021, 11, e1493.

55. Bannwarth, C.; Ehlert, S.; Grimme, S. GFN2-xTB—An Accurate and Broadly Parametrized Self-Consistent Tight-Binding Quantum Chemical Method with Multipole Electrostatics and Density-Dependent Dispersion Contributions. J. Chem. Theory Comput. 2019, 15, 1652–1671.